Electronic Supporting Information

Understanding Three-Dimensionally Interconnected Porous Oxide-Derived Copper Electrocatalyst for Selective Carbon Dioxide Reduction†

Thuy-Duong Nguyen-Phan,*[a,b] Congjun Wang,[a,b] Chris M. Marin,[a,b] Yunyun Zhou,[a] Eli Stavitski,[c] Eric J. Popczun,[a] Yang Yu,[a] Wenqian Xu,[d] Bret H. Howard,[a] Mengling Y. Stuckman,[a,b] Iradwikanari Waluyo,[c] Paul R. Ohodnicki Jr.[a] and Douglas R. Kauffman*[a]

[a] National Energy Technology Laboratory, 626 Cochrans Mill Road, P.O. Box 10940, Pittsburgh, PA 15236-0940, USA

[b] Leidos Research Support Team, 626 Cochrans Mill Road, P.O. Box 10940, Pittsburgh, PA 15236-0940, USA

[c] Photon Sciences Division, National Synchrotron Light Source II, Brookhaven National Laboratory, Upton, New York 11973, USA

[d] X-ray Science Division, Advanced Photon Source, Argonne National Laboratory, Argonne, Illinois 60439, USA

* ThuyDuong.NguyenPhan@netl.doe.gov; Douglas.Kauffman@netl.doe.gov

I. EXPERIMENTAL SECTION

Chemicals

Methyl methacrylate ($CH_2=C(CH_3)COOCH_3$), 2,2'-azobis (2-methylpropionamidine) dihydrochloride ($[=NC(CH_3)_2C(=NH)NH_2]_2.2HCl$), sodium hydroxide (NaOH), copper (II) nitrate trihydrate ($Cu(NO_3)_2.3H_2O$), citric acid monohydrate ($C_6H_8O_7.H_2O$), acetone (($CH_3)_2CO$), isopropanol (C_3H_7OH), and absolute ethanol (C_2H_5OH) were purchased from Sigma-Aldrich. All chemicals were used as received without further purification. Ultra-pure deionized water (DIW) with 18.3 $M\Omega$ cm^{-1} resistivity (Barnstead EASYpure LF) was used in all synthetic and electrochemical experiments.

1. Synthesis of poly (methyl methacrylate) (PMMA) latex and PMMA opal films

PMMA latex was prepared by surfactant-free emulsion polymerization using a cationic free radical initiator. DIW (875 mL) and methyl methacrylate (100 g) were mixed at room temperature under a nitrogen flow for 30 min and then maintained at 70 °C. Subsequently, a solution containing 0.15 g of 2,2'-azobis (2-methylpropionamidine) dihydrochloride and 25 mL of DIW was quickly added. The milky white suspension was formed, and the suspension was maintained at 70 °C for 6 h to complete the polymerization. After cooling down to room temperature for 1 h, the concentration of obtained PMMA latex (diameter of *ca.* 210 nm) was 10 wt%.

Bare glass substrates were cut into 1 cm x 3 cm pieces and cleaned with a mixture of acetone, isopropanol and DIW for two hours and then immersed in aqueous sodium hydroxide solution (0.5 M) for at least six hours to hydrophilize the surface. The hydrophilized substrates were finally rinsed by DIW and dried under N_2 flow.

PMMA opal films were grown by the evaporation-induced vertical deposition technique. The stock PMMA colloidal suspension was diluted in DIW to achieve the concentration of 0.5 wt%. The hydrophilized substrate was partially immersed into 5 mL of PMMA solution with an angle of

45 ~ 60° and left in an electric oven at 35 °C with controlled humidity of ~80% for several days to form a self-assembled opal in a *fcc* crystalline lattice over an area of 1 cm x 1.5 cm. The opal film was then sintered at 80 °C for 30 minutes to enhance the domain arrangement and mechanical stability.

2. Materials characterization

X-ray photoelectron spectroscopy (XPS) of fresh catalysts was carried out on a PHI 5600ci spectrometer using Al Kα (1486.6 eV) radiation source and a hemispherical analyzer. The XPS spectra of the post-reaction electrodes were collected on a PHI 5000 VersaProbe III scanning XPS microprobe (Physical Electronics, ULVAC-PHI Inc) using Al Kα (1486.6 eV) radiation source and a hemispherical analyzer. All the binding energies was internally calibrated to the C 1s peak of surface adventitious carbon at 284.6 eV.

Ex situ soft X-ray absorption spectra (s-XAS) were obtained at beamline 23-ID-2 (IOS) of the NSLS-II, BNL. Powder samples were mounted on sample holder with carbon tape and loaded into the analysis chamber. Cu L-edge was collected using total electron yield (TEY) detection mode. The spectrum was normalized and analyzed using Athena module of IFEFFIT package.[1]

3. Calculation of Faradaic efficiency

The Faradaic efficiency for product *i* was calculated using the following equations:

$$FE_i\,(\%) = \frac{moles\ of\ product\ i\ x\ number\ of\ electrons\ needed\ for\ producing\ i}{total\ number\ of\ electrons\ passed}\ x\ 100\%$$

$$FE_i = \frac{z_i * F * n_i}{I * t}$$

where z_i is the number of electrons involved in the formation of *i* product (z = 2 for CO, H_2, and HCOOH, z = 8 for CH_4, z = 12 for C_2H_4, and z = 14 for C_2H_6); *F* is the Faraday's constant; n_i is the

number of moles of product i formed (determined by GC and IC); I is the total current; and t is electrolysis time.

4. Determination of electrochemical surface area (ECSA) and surface roughness factor (RF)

The ECSA of all the electrocatalysts was estimated from the electrochemical double layer capacitance (C_{dl}). Cyclic voltammetry was performed between 0.15 and 0.35 V *vs.* RHE (where there are no Faradaic process occurring) at various scan rates in CO_2-saturaed 0.1 M $KHCO_3$ electrolyte. C_{dl} was extracted from the plot of capacitive currents against scan rates and the ECSA was calculated against the specific capacitance for smooth Cu surface (29 $\mu F \ cm^{-2}$).[2,3] The RFs were determined by dividing ECSA values by the geometric electrode area.

II. SUPPORTING TABLES

Table S1. Potential dependent Faradaic efficiencies (FE, %) and formation rate (r, mmol $g_{catalyst}^{-1}$ h^{-1}) of EC-CO$_2$RR products for CuO-IO.

V vs. RHE	CO FE	CO r	CH$_4$ FE	CH$_4$ r	C$_2$H$_4$ FE	C$_2$H$_4$ r	C$_2$H$_6$ FE	C$_2$H$_6$ r	HCOOH FE	HCOOH r	H$_2$ FE	H$_2$ r
-1.2	31.1	64.2	6.7	0.7	1.9	0.7	<0.1	6.6×10^{-3}	25.6	39.7	20.4	50.1
-1.1	36.1	59.2	17.6	7.2	2.8	0.78	-	-	23.3	22.9	10.5	17.3
-1.0	54.9	68.0	16.0	5.3	3.6	0.9	-	-	11.4	11. 3	4.3	6.1
-0.9	49.1	43.5	7.2	1.5	0.45	5.8×10^{-2}	-	-	14.7	11.7	5.7	4.5
-0.8	63.2	28.2	2.7	0.3	-	-	-	-	7.8	3.9	-	-
-0.7	66.5	16.1	1.8	0.1	-	-	-	-	5.5	1.9	-	-
-0.6	72.5	8.6	1.0	2.9×10^{-2}	-	-	-	-	9.2	2.9	-	-
-0.5	59.3	3.00	1.9	2.4×10^{-2}	-	-	-	-	13.6	1.8	-	-
-0.4	48.2	0.8	7.0	2.7×10^{-2}	-	-	-	-	23.2	0.5	-	-
-0.3	22.7	0.2	18.9	3.1×10^{-2}	-	-	-	-	48.1	0.3	-	-
-0.2	9.7	3.1×10^{-2}	40.7	3.1×10^{-2}	-	-	-	-	21.8	0.1	-	-

Table S2. Potential dependent Faradaic efficiencies (FE, %) and formation rate (r, mmol $g_{catalyst}^{-1}$ h^{-1}) of EC-CO$_2$RR products for bulk CuO.

V vs. RHE	CO		CH$_4$		C$_2$H$_4$		C$_2$H$_6$		HCOOH		H$_2$	
	FE	r	FE	r	FE	r	FE	r	FE	r	FE	r
-1.2	4.7	6.0	4.4	1.4	15.2	3.2	0.1	2.3×10^{-2}	5.8	17.4	57.7	73.5
-1.1	7.6	7.3	2.3	0.6	20.8	3.3	0.4	4.8×10^{-2}	12.6	18.6	60.4	58.2
-1.0	9.0	6.1	0.5	9.1×10^{-2}	16.1	1.8	0.7	6.8×10^{-2}	12.0	9.9	71.0	47.9
-0.9	11.1	5.0	0.3	3.4×10^{-2}	11.6	0.9	1.2	8.0×10^{-2}	7.4	3.7	87.9	39.9
-0.8	13.4	4.3	0.4	3.2×10^{-2}	4.7	0.3	1.2	5.2×10^{-2}	11.4	3.1	79.0	25.1
-0.7	10.3	2.1	0.5	2.4×10^{-2}	0.9	3.2×10^{-2}	0.4	1.2×10^{-2}	12.9	2.1	65.8	13.6
-0.6	16.8	2.4	0.6	2.1×10^{-2}	-	-	-	-	7.3	0.8	65.2	9.2
-0.5	15.8	1.1	2.0	3.3×10^{-2}	-	-	-	-	9.6	0.4	55.3	3.7
-0.4	14.3	0.4	2.2	1.4×10^{-2}	-	-	-	-	8.6	0.3	51.0	1.4
-0.3	7.8	6.2×10^{-2}	5.2	1.0×10^{-2}	-	-	-	-	8.1	0.2	-	-
-0.2	1.6	4.6×10^{-3}	7.1	5.1×10^{-3}	-	-	-	-	5.5	0.1	-	-

**Table S3.** Potential dependent Faradaic efficiencies (FE, %) and formation rate (r, mmol $g_{catalyst}^{-1}$ h^{-1}) of EC-CO_2RR products for CuO NPs.

V vs.	CO		CH_4		C_2H_4		C_2H_6		HCOOH		H_2	
RHE	FE	r	FE	r	FE	r	FE	r	FE	r	FE	r
-1.2	5.9	10.2	5.3	2.3	15.6	4.5	0.1	3.2×10^{-2}	12.6	30.3	64.4	110.5
-1.1	7.7	9.6	2.0	0.6	13.5	2.8	0.1	2.3×10^{-2}	21.0	25.9	59.4	74.0
-1.0	9.1	7.6	0.5	1.1	11.4	1.6	0.2	21.8×10^{-2}	19.2	15.9	60.0	50.0
-0.9	13.1	4.7	0.4	3.3×10^{-2}	4.9	0.3	-	-	18.6	9.9	62.2	22.5
-0.8	14.5	3.0	0.3	1.7×10^{-2}	2.0	6.7×10^{-2}	-	-	9.7	3.3	73.8	15.0
-0.7	18.2	1.8	0.7	1.8×10^{-2}	-	-	-	-	8.3	1.4	76.7	7.6
-0.6	14.2	0.8	1.6	2.3×10^{-2}	-	-	-	-	5.2	0.5	80.4	4.7
-0.5	6.2	0.2	3.0	2.2×10^{-2}	-	-	-	-	10.6	0.4	82.8	2.5
-0.4	6.3	7.2×10^{-2}	10.8	3.1×10^{-2}	-	-	-	-	20.9	0.4	67.6	0.8
-0.3	3.7	1.6×10^{-2}	13.5	1.4×10^{-2}	-	-	-	-	27.5	0.3	59.1	0.3
-0.2	2.0	3.5×10^{-3}	22.1	9.5×10^{-3}	-	-	-	-	29.1	0.2	-	-

Table S4. Comparison of CO_2 conversion to C_1 products of present study and previous oxide-derived Cu and Cu based catalyst reports.

Sample	Major C_1 product	FE / %	Potential / V *vs.* RHE	References
CuO-derived Cu inverse opal	CO	72.5	-0.6	This work
	HCOOH	48.1	-0.3	
Cu$_2$O-derived Cu	CO	45	-0.35	Li et al., J. Am. Chem. Soc. 2012, 134, 7231-7234
	HCOOH	38	-0.55	
Chrysanthemum-like Cu nanoflower	HCOOH	50 ~ 70	-1.6	Xie et al., Electrochimica Acta 2014, 139 137-144
CuO-derived Cu nanowire	CO	50	-0.6	Ma et al., Phys. Chem. Chem. Phys. 2015, 17, 20861-20867
	HCOOH	40	-0.7	
Electrochemically reduced CuO-derived Cu nanowire	CO	61.8	-0.4	Raciti et al., Nano Lett. 2015, 15, 6829-6835
	HCOOH	30.7	-0.6	
Electrochemically reduced CuO-derived Cu nanowire	CO	62	-0.4	Cao et al., ACS Catal. 2017, 7, 8578-8587
	HCOOH	25	-0.5	
Cu$_2$O-derived Cu inverse opal	CO	45.3	-0.6	Zheng et al., Nano Energy 2018, 48, 93-100
	HCOOH	34.5	-0.8	

3D CuO-derived Cu hierarchical nanostructures	CO	60	-0.55	Raciti et al., ACS Appl. Energy Mater. 2018, 1, 2392-2398
	HCOOH	30 ~ 40	-0.55 ~ -0.7	
Cu nanoparticles/N-doped carbon nanospike	CO	23	-0.7	Song et al., ChemistrySelect 2016, 1, 6055-6061
	CH_4	35	-0.9	
Cu nanoparticles/reduced graphene oxide	CO	~40	-0.6	Hossain et al., Sci. Rep. 2017, 7, 3184
	HCOOH	46.2	-0.4	
Cu nanoparticles/reduced graphene oxide	CO	50	~ -0.4	Cao et al., J. CO_2 Util. 2017, 22, 231-237
Cu/carbon aerogels	CO	35	-0.81	Han et al., Electrochim. Acta 2019, 297, 545-552
Cu nanoparticles/carbon aerogels	CO	75.6	-0.6	Xiao et al., J. Colloid Interface Sci. 2019, 545, 1-7

Table S5. ECSA and RF of as-prepared CuO-IO, bulk CuO and CuO NPs electrodes.

Sample	ECSA / cm^2	RF
CuO-HIO	2.962	30.79
Bulk CuO	0.372	5.27
CuO nps	0.548	7.76

III. SUPPORTING FIGURES
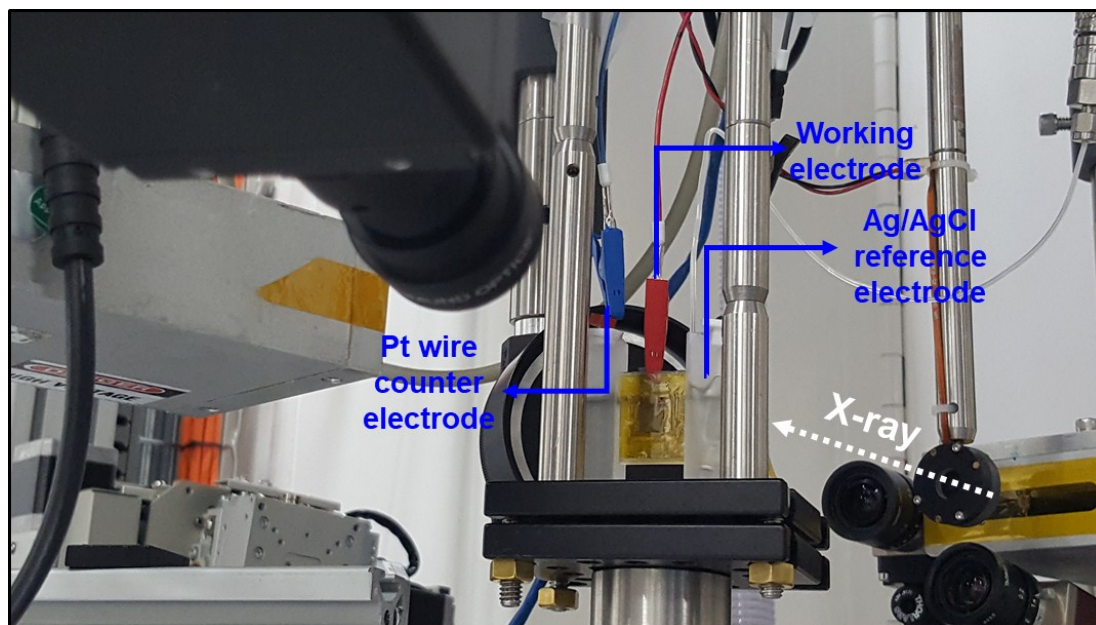
Fig. S1. Experimental setup for *in situ* XAFS experiment.
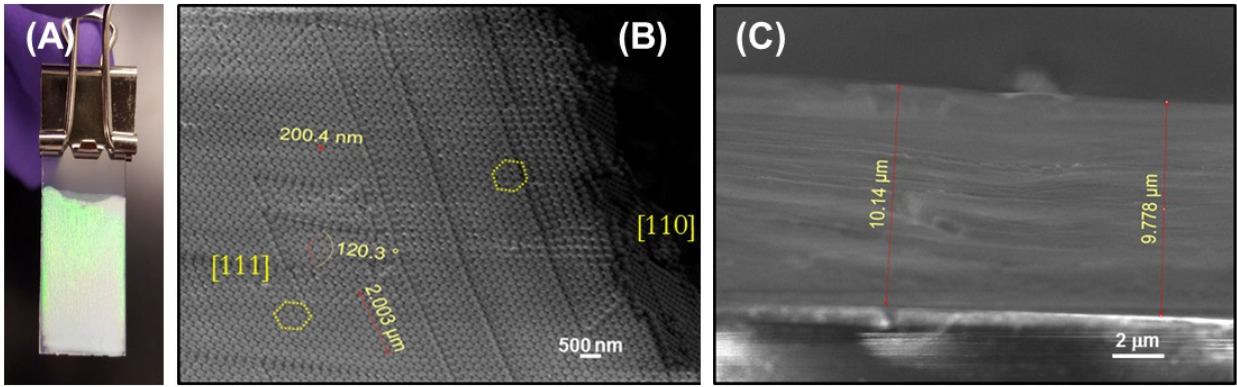
Fig. S2. (A) Photographs of PMMA film on ITO substrate, (B) top-view and (C) cross-sectional SEM images of PMMA dry opal film.

A typical photograph of PMMA opal template on glass substrate shows a striking bright green color arising from Bragg reflection of incident light from long-range ordering. Top view SEM image indicates 3D ordered hexagonal arrangement of PMMA spheres with diameter of ~ 200 nm in periodic close-packed (111) face-centered cubic dry opal. The thickness of PMMA film was about 10 μm.
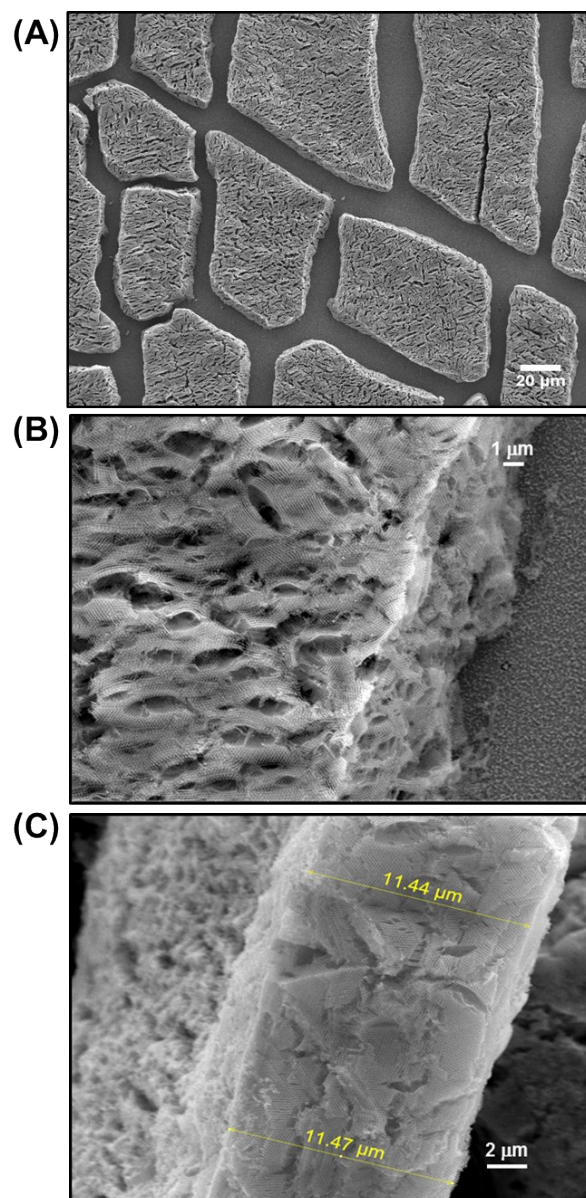
Fig. S3. (A, B) Top-view and (C) cross-sectional SEM images of as-prepared CuO-IO catalyst layer on hydrophilized glass substrate.

SEM images show the successful filling of the interstitial void of PMMA with a CuO backbone in a *fcc* lattice. The average cavity size of 180±5 nm is slightly smaller than that of PMMA spheres due to the shrinkage upon calcination. The images imply the high homogeneity of CuO-IO over more than 20 μm^2 area and the average thickness of CuO-IO layer on glass is approximately 12 μm.
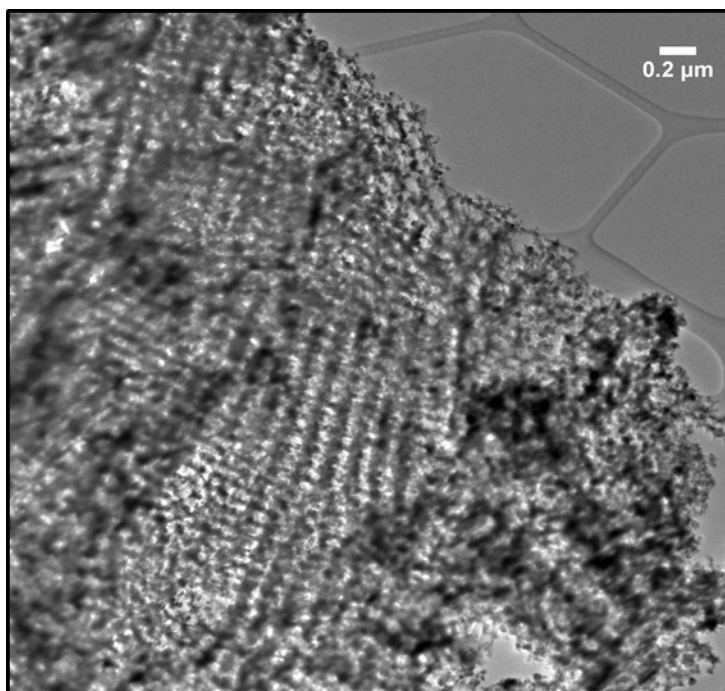
Fig. S4. Low magnification TEM image of as-prepared CuO-IO.
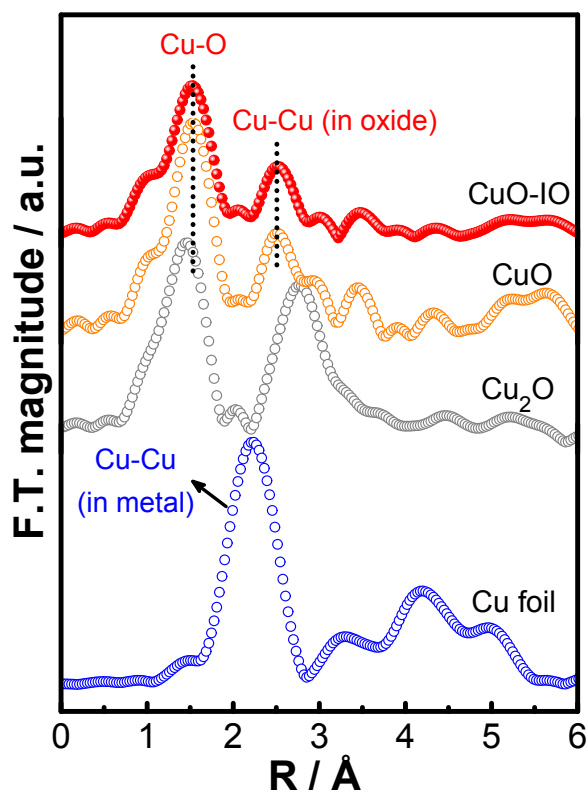
Fig. S5. Fourier-transformed R-space Cu K-edge EXAFS spectra (not phase corrected) of as-prepared CuO-IO, bulk CuO, bulk Cu_2O and Cu foil standards.
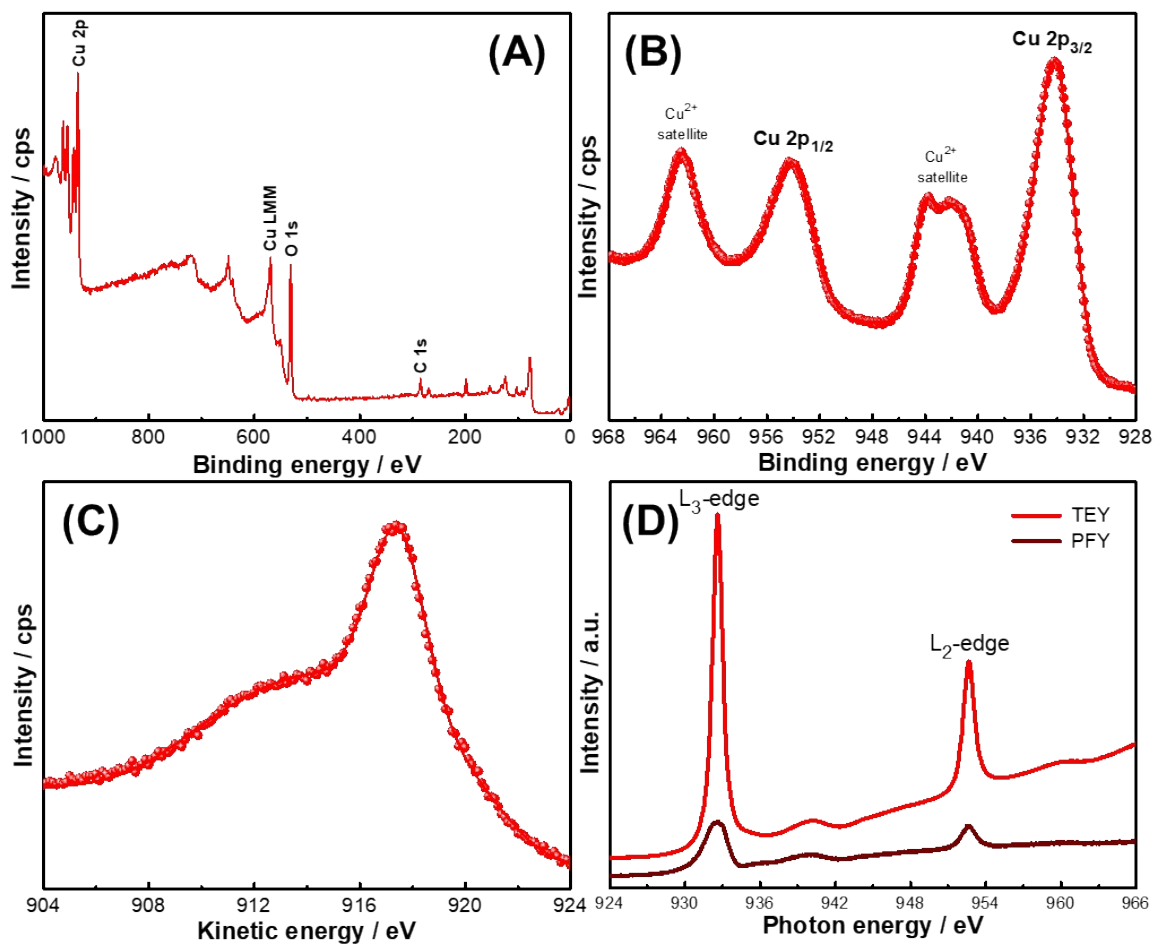
Fig. S6. (A) XPS survey, (B) Cu 2p core-level, and (C) Auger Cu LMM, and (D) s-XAS Cu L-edge (in TEY and PFY modes) spectra of as-prepared CuO-IO confirmed the presence of Cu^{2+}.
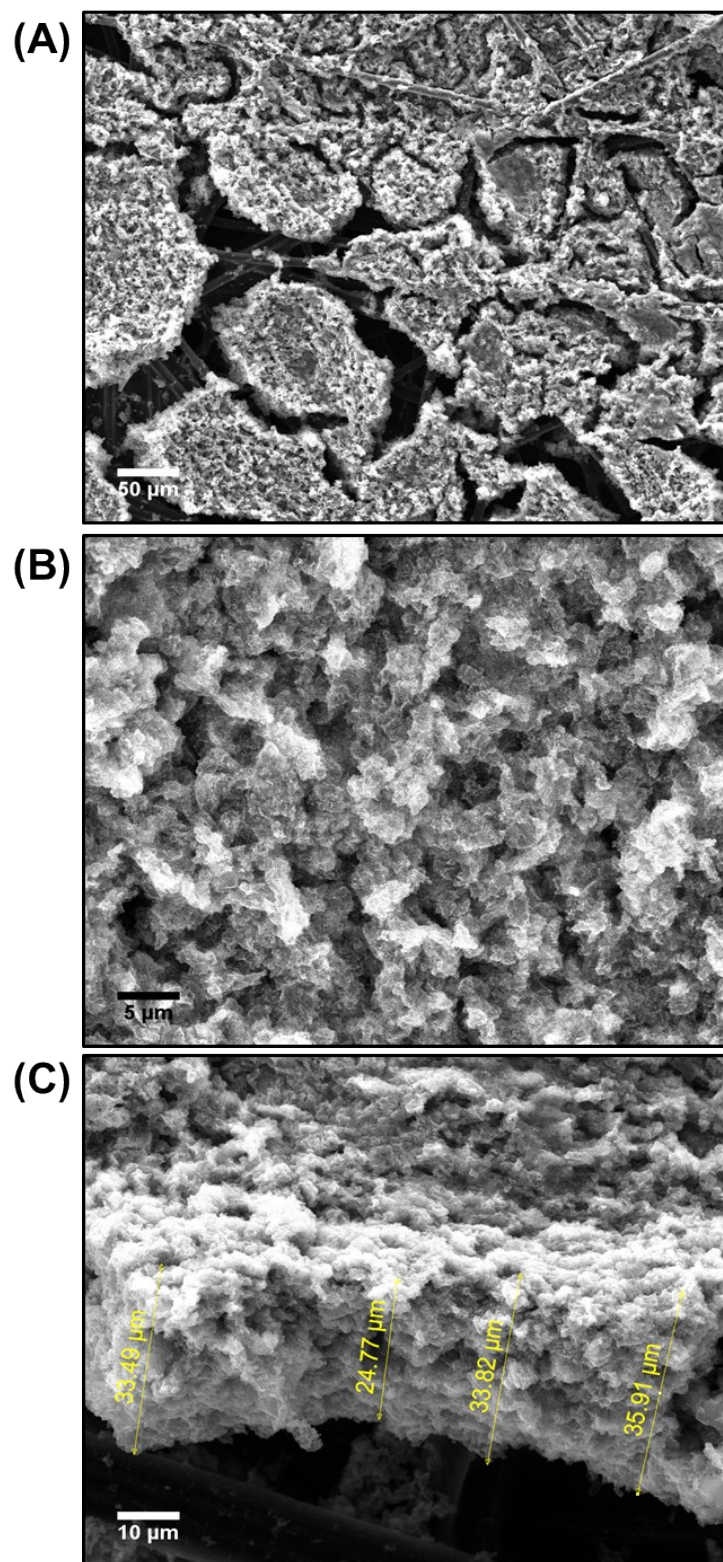
Fig. S7. (A, B) Top-view and (C) cross-sectional SEM images of CuO/Nafion/carbon paper working electrode (2.8 mg cm^{-2} loading).
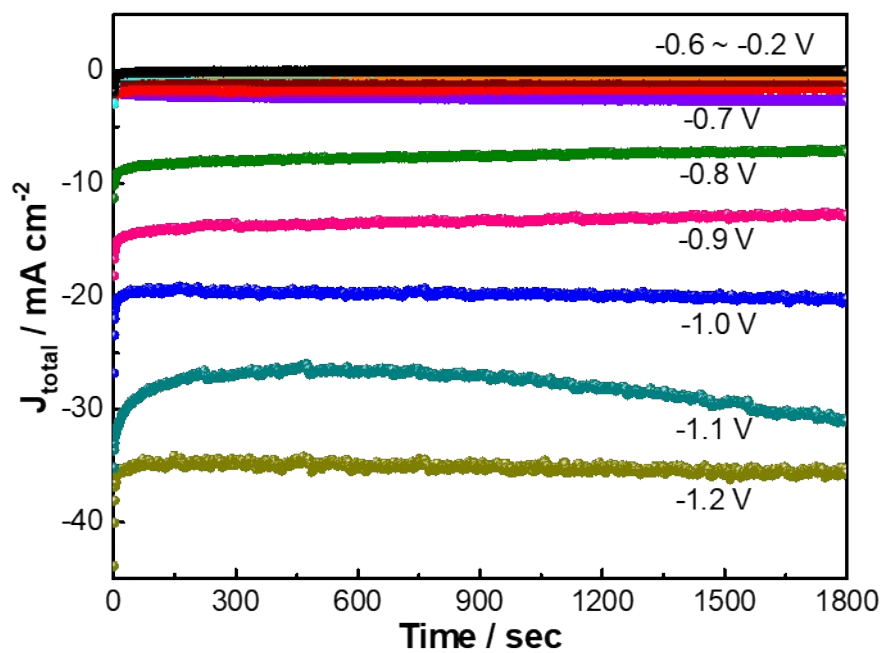
Fig. S8. Chronoamperometric profiles showing total current density as function of applied constant potential for CuO-IO catalyst (loading of 2.8 mg cm_{geo}^{-2}).
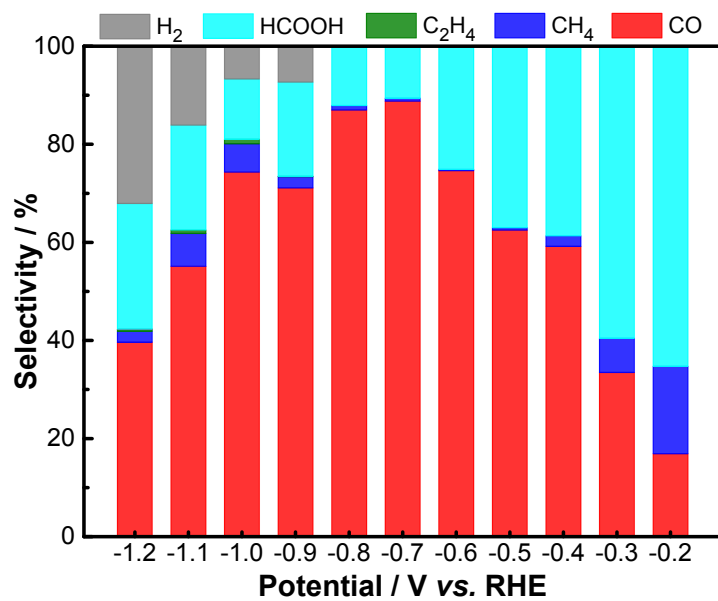
Fig. S9. Selectivity of CO_2 reduction products for CuO-IO catalyst at different applied potentials.
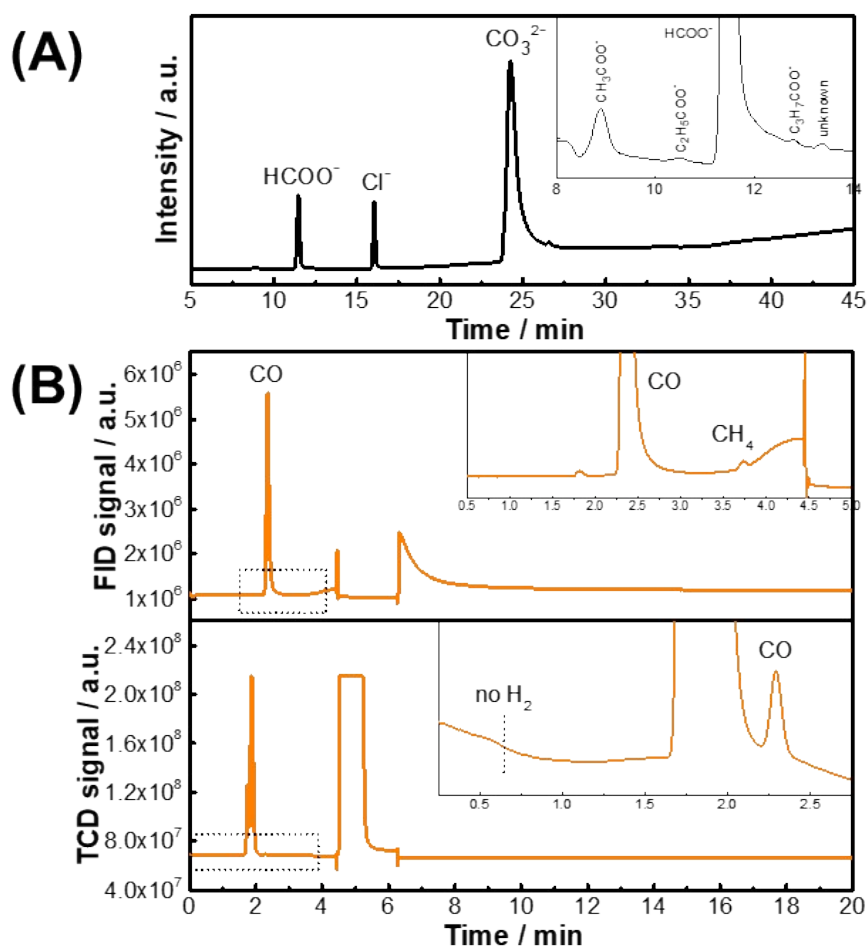
Fig. S10. (A) Representative ion chromatography spectra for liquid product analysis at -1.2 V *vs.* RHE (diluted 10 times); and (B) gas chromatography spectra for gas product analysis at -0.6 V *vs.* RHE: (upper) FID and (low) TCD signal (taken for CuO-IO catalyst).
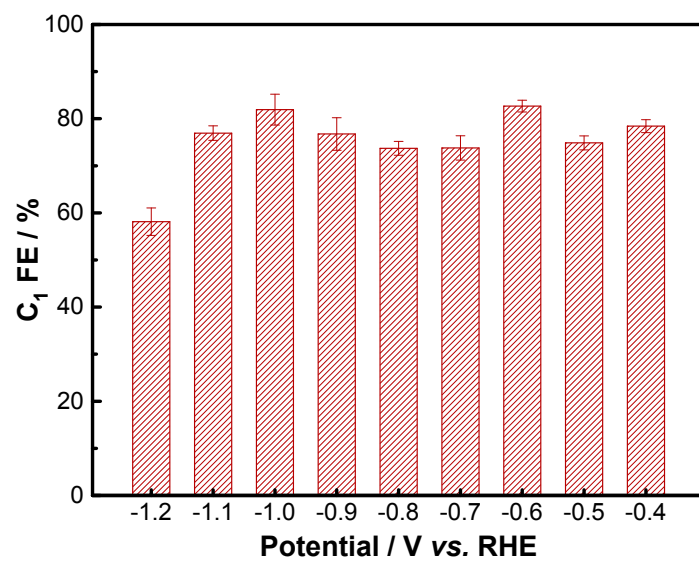
Fig. S11. Total Faradaic efficiency for C_1 products at various applied potentials of CuO-IO catalyst.
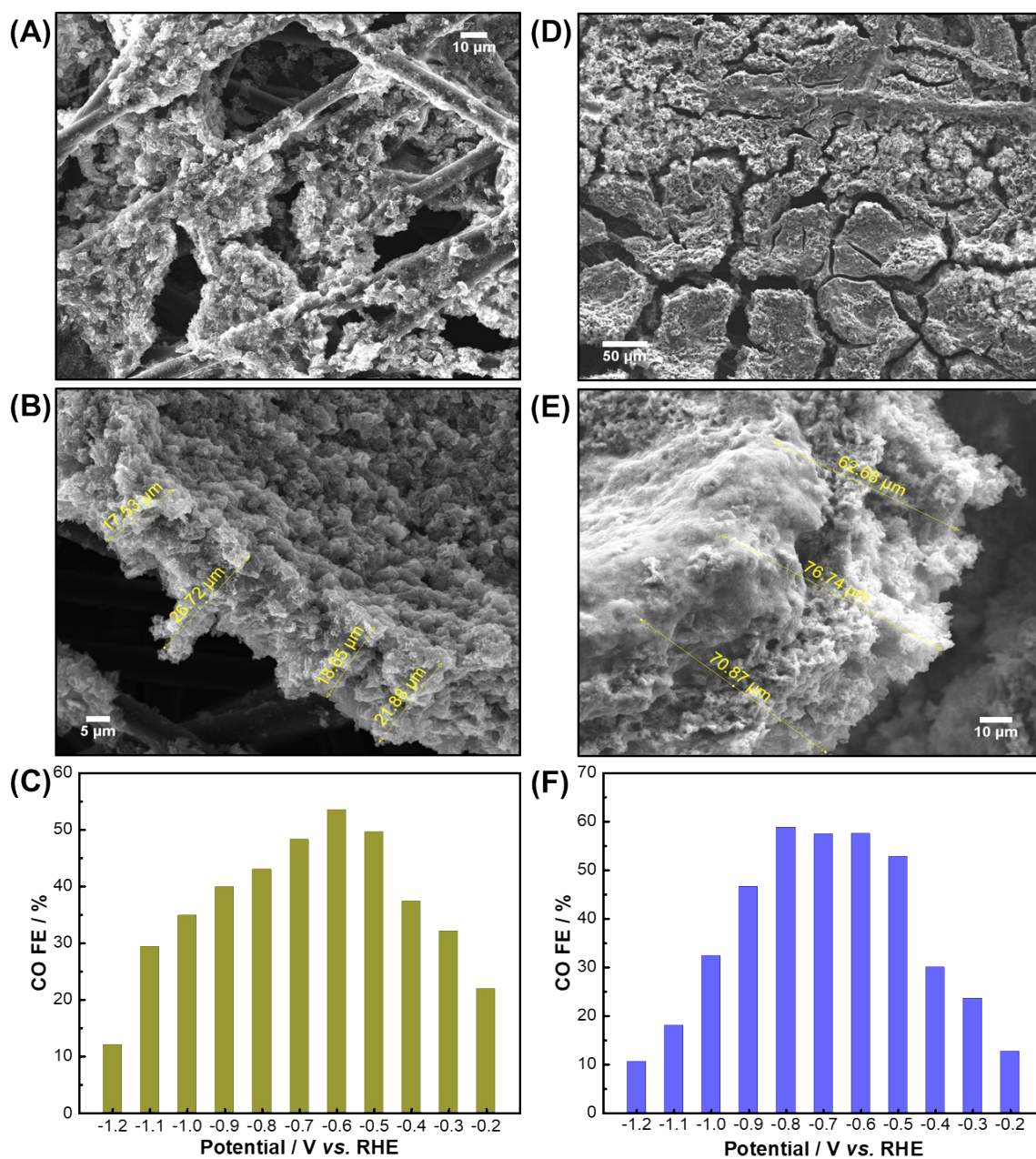
Fig. S12. SEM images of CuO-IO/carbon paper working electrodes with CuO-IO loading of (A, B) 1.5 mg cm$_{geo}^{-2}$ and (D, E) 15 mg cm$_{geo}^{-2}$; and (C, F) corresponding CO FE $vs.$ applied potentials.
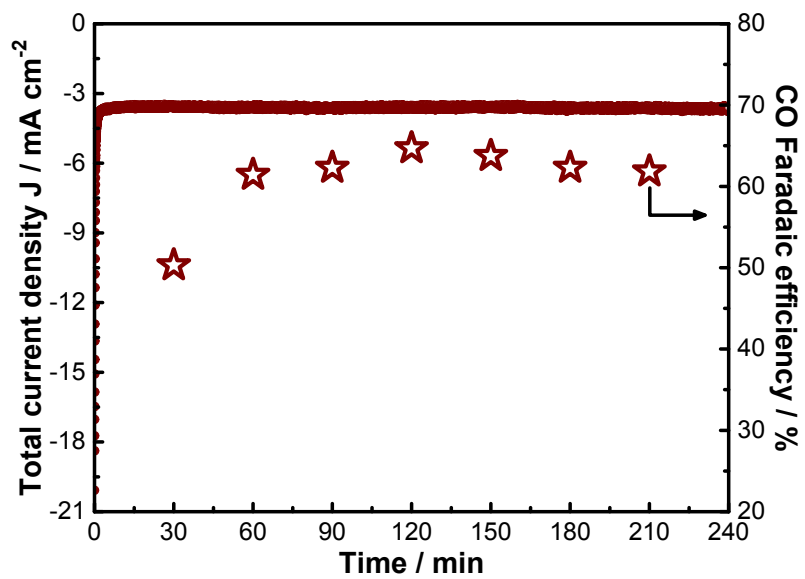
Fig. S13. Steady-state current density and FE for CO production at -0.6 V *vs.* RHE as using graphite counter electrode (in CO_2-saturated $KHCO_3$, CO_2 flow rate of 20 mL min^{-1}, catalyst loading of 2.8 mg cm_{geo}^{-2}).
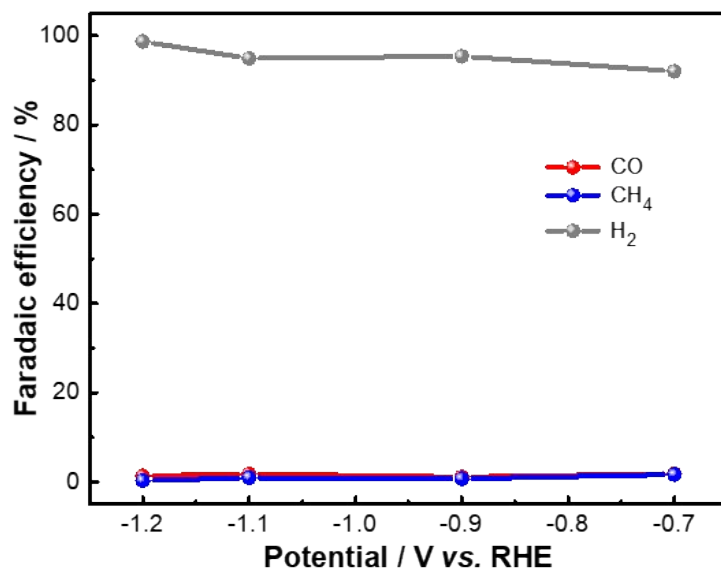
Fig. S14. Faradaic efficiency for CO, CH$_4$ and H$_2$ at different cathodic potentials over bare carbon paper (in CO$_2$-saturated KHCO$_3$ electrolyte, CO$_2$ flow rate of 20 mL min^{-1}).
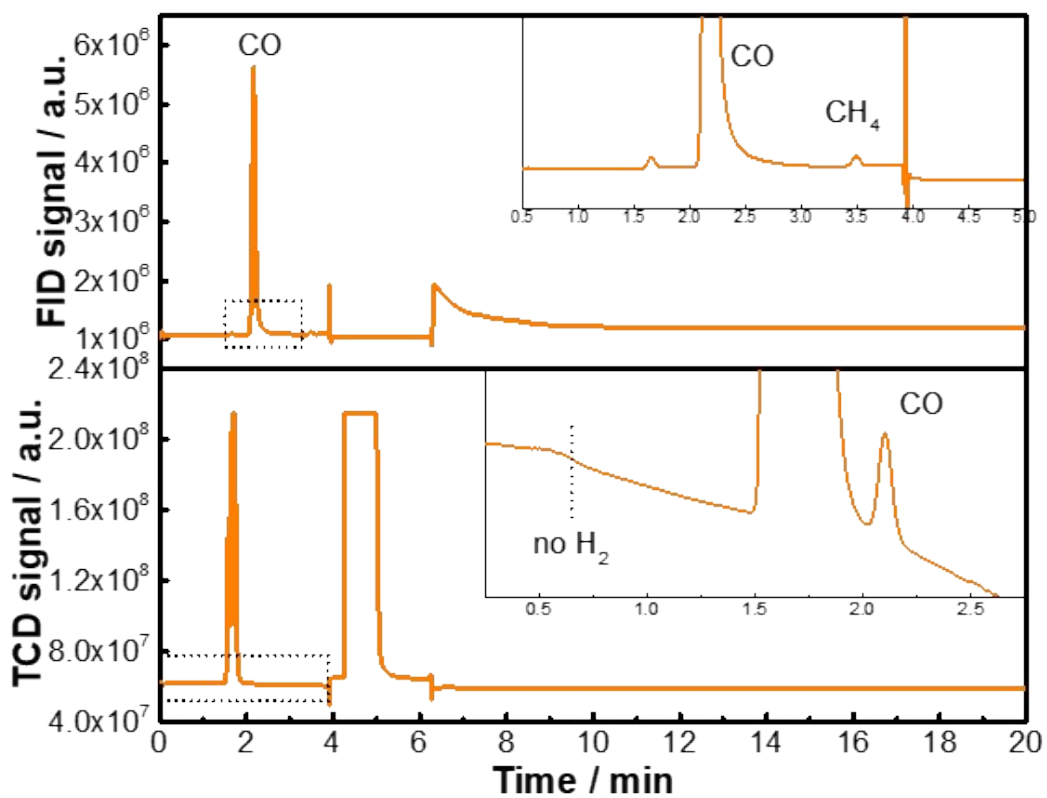
Fig. S15. Representative gas chromatography spectra for gas product analysis after 24-h electrolysis at -0.6 V *vs.* RHE: (upper) FID and (low) TCD signal (taken for CuO-IO catalyst).
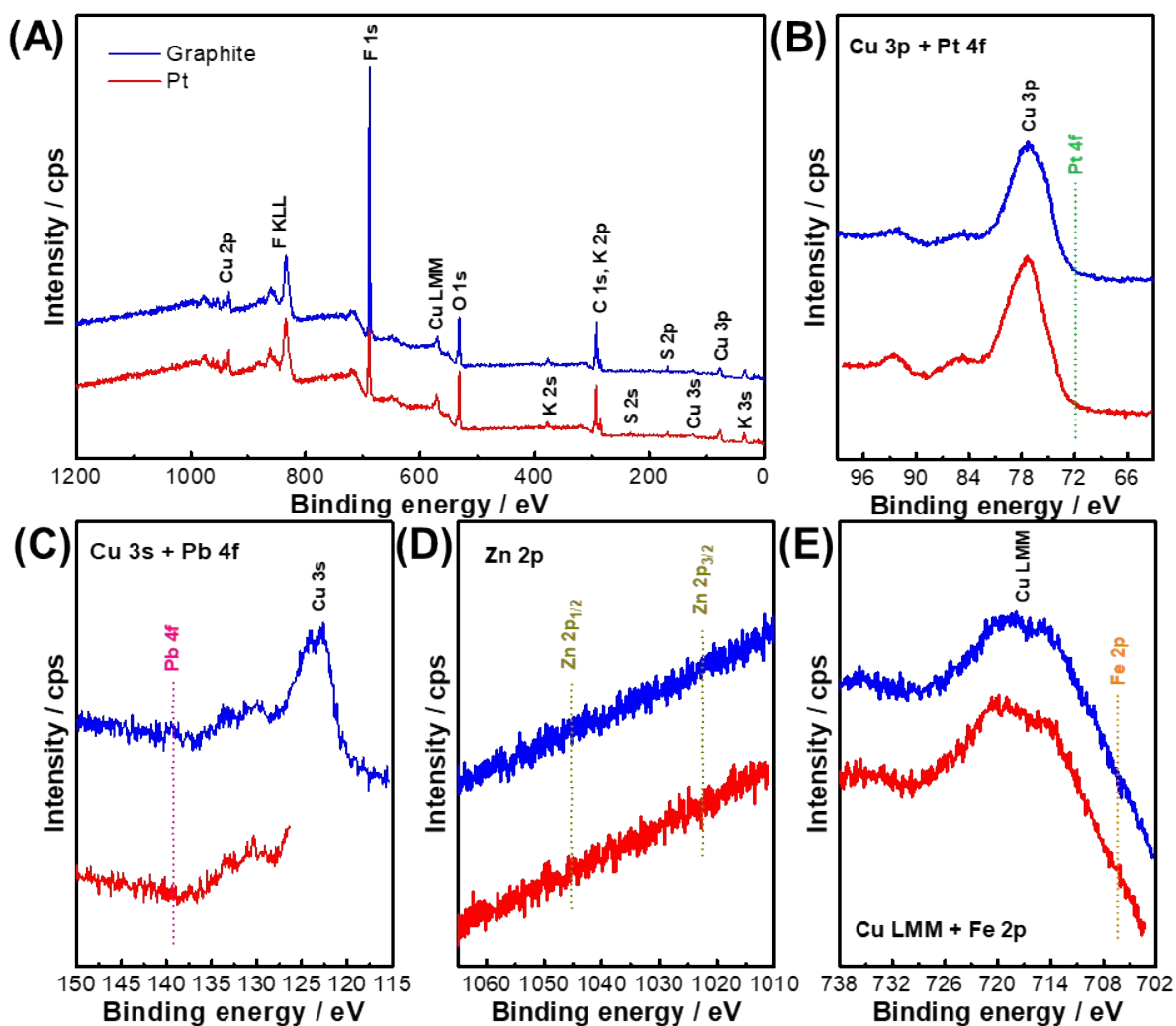
Fig. S16. (A) XPS survey, (B) Cu 3p - Pt 4f, (C) Cu 3s - Pb 4f, (D) Zn 2p, and (E) Fe 2p core-level spectra of CuO-HIO post-electrodes after long-term run at -0.6 V *vs.* RHE using Pt wire (red) and graphite (blue) counter electrodes.
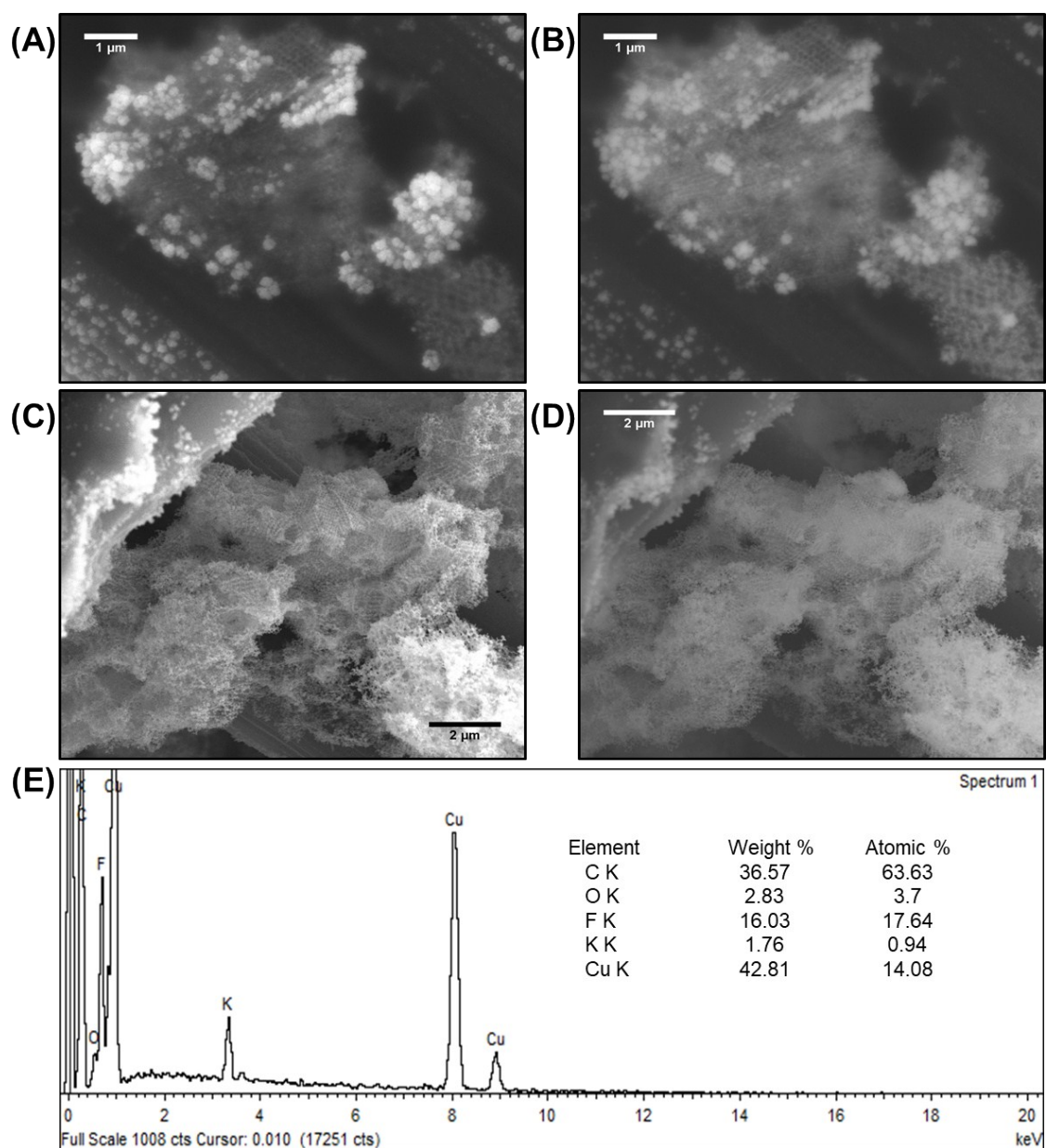
Fig. S17. (A-D) SEM images of CuO-IO electrode at different spots after 24-hour electrolysis at -0.6 V *vs.* RHE show that CuO-IO retained its structure after durability test despite partial structural dissolution into nanoparticle agglomerates (occupying approximately 20-30% of entire post-electrode). (E) EDX analysis identified the presence of Cu, carbon and fluorine from the PTFE-coated Toray carbon paper and Nafion binder, and potassium from the $KHCO_3$ electrolyte. Post-reaction EDX did not identify Pt.
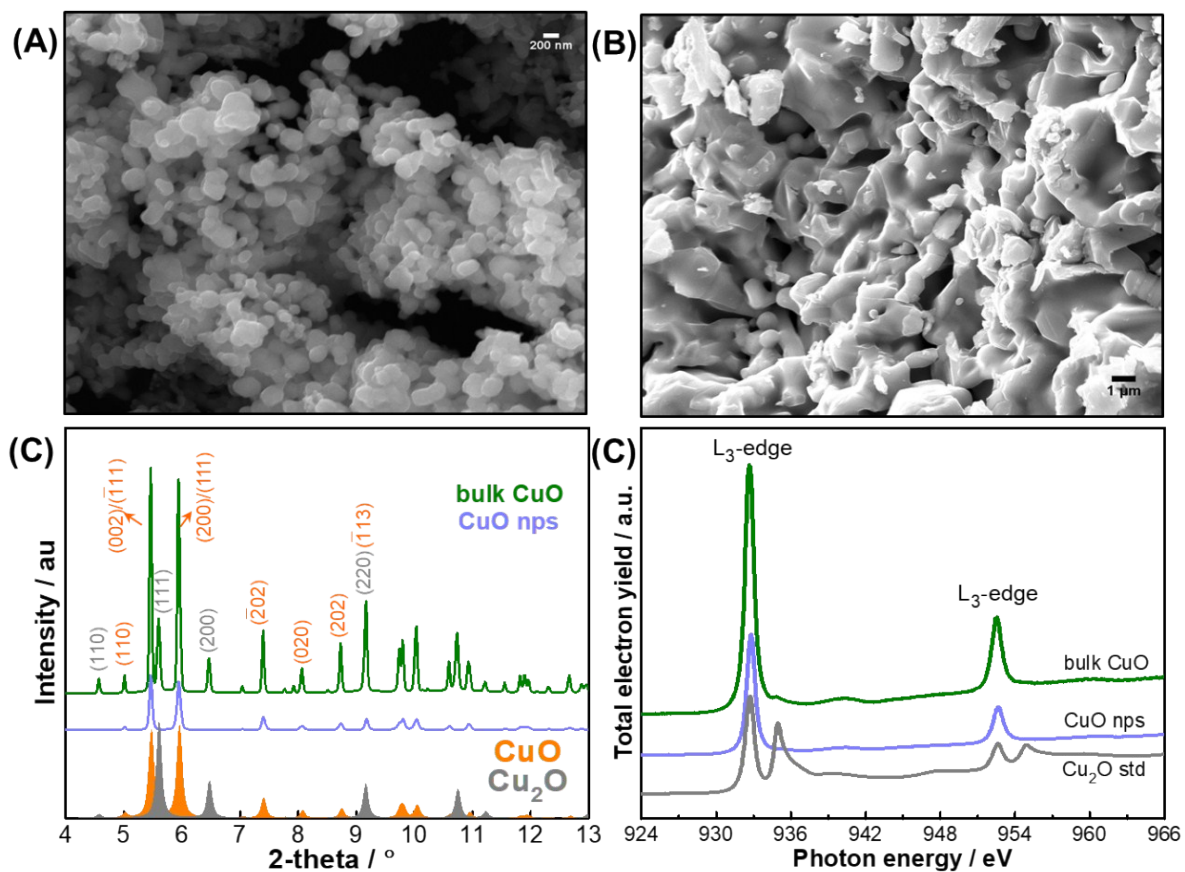
Fig. S18. (A, B) SEM images, (C) XRD patterns, and (D) Cu L-edge XAS of CuO NPs and bulk CuO. The spectra clearly show high crystallinity of monoclinic cuprous oxide of both CuO NPs (~50 nm diameter) and bulk CuO (~1-5 μm). Mixture of CuO and cubic Cu_2O was detected in bulk CuO powder.
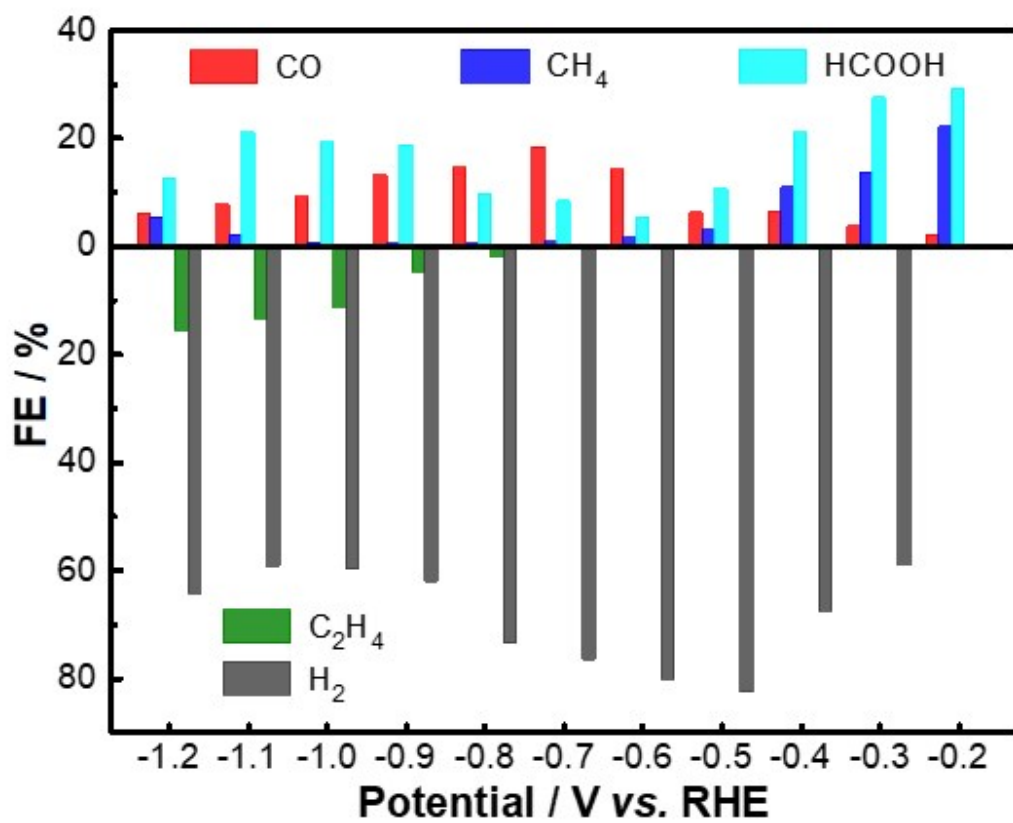
Fig. S19. Faradaic efficiency for EC-CO$_2$RR products as a function of potentials for ~ 50 nm diameter CuO NPs.
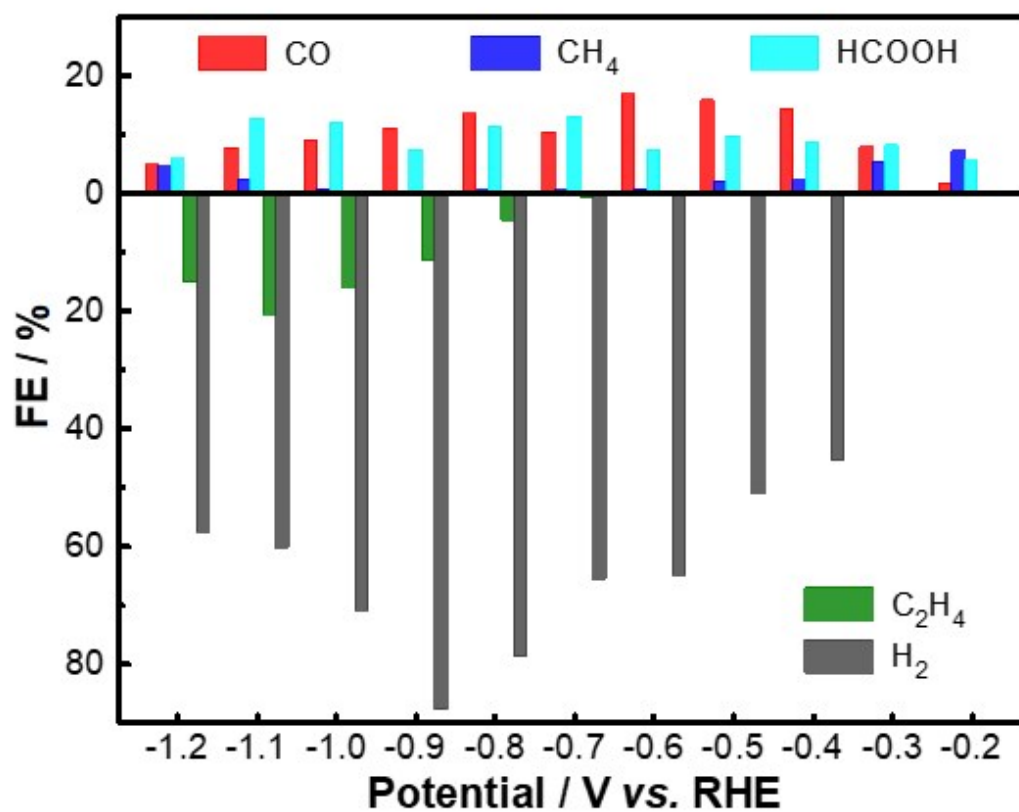
Fig. S20. Faradaic efficiency for EC-CO$_2$RR products as a function of potentials for bulk CuO powder.
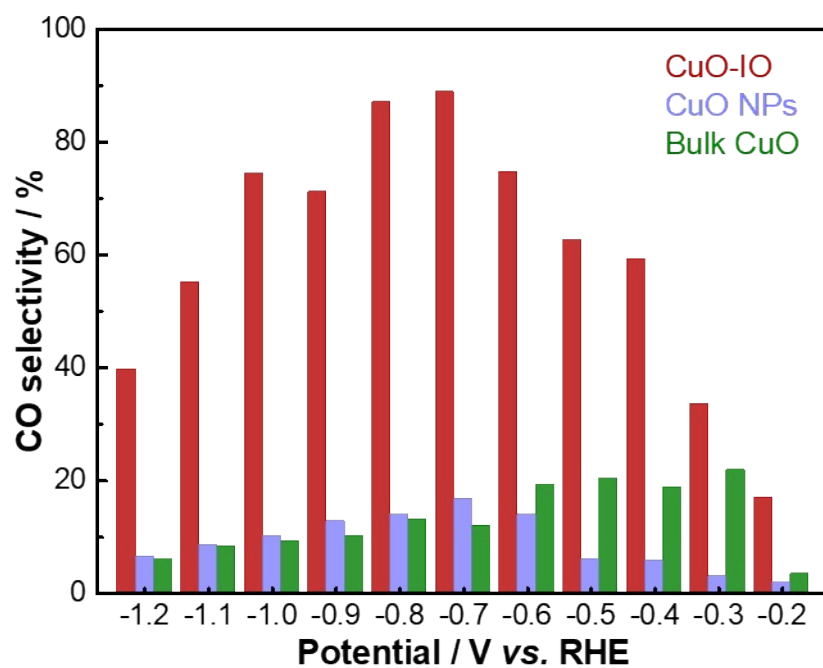
Fig. S21. CO selectivity at various negative potentials for CuO-IO, ~50 nm diameter CuO NPs, and bulk CuO powder.
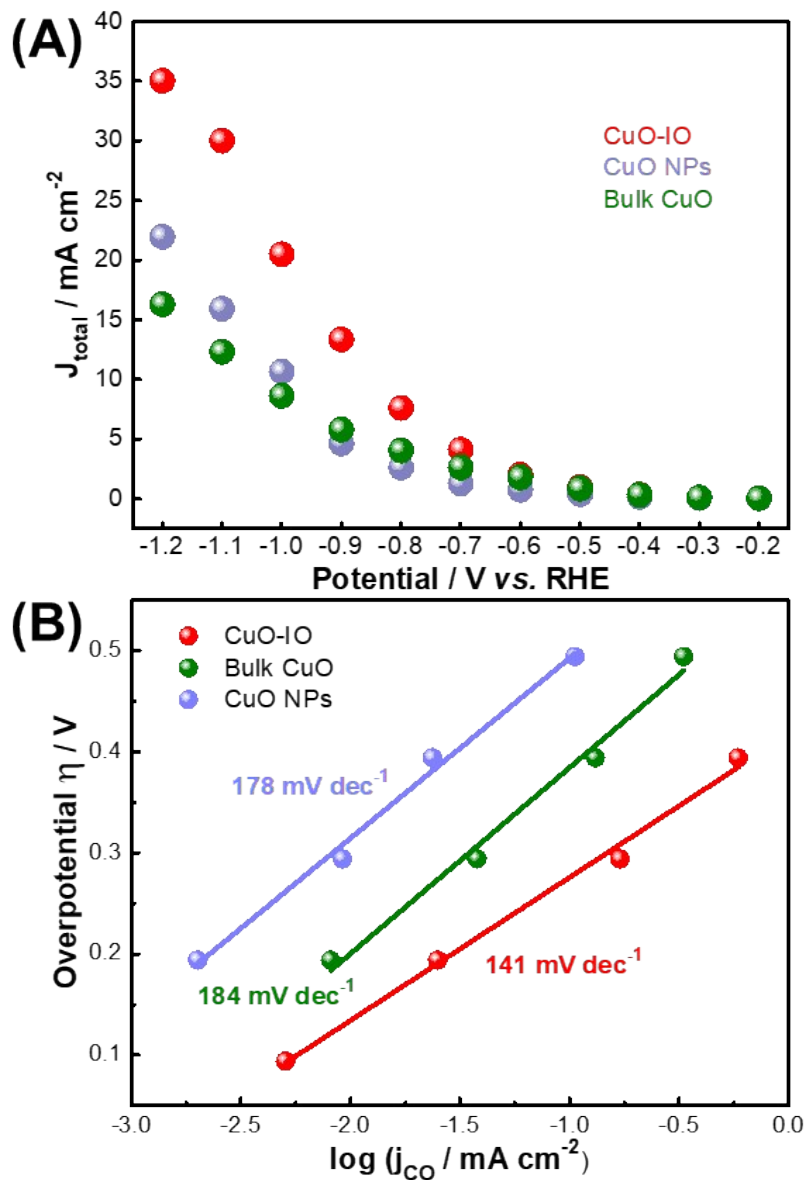
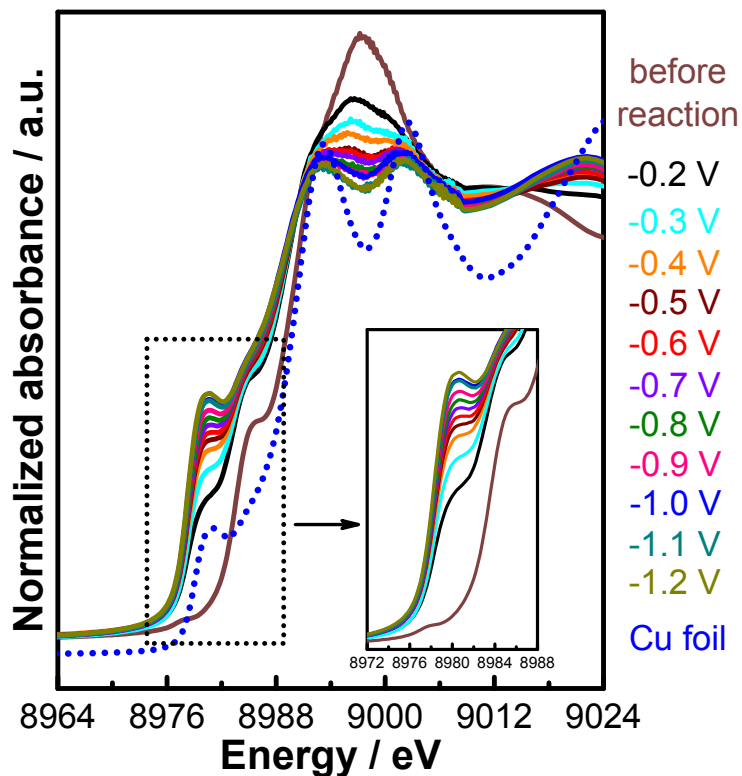**Fig. S22.** (A) Total current density *vs.* cathodic potential and (B) Tafel plot for CO production over CuO-IO, ~50 nm CuO NPs, and bulk CuO powder.

Fig. S23. *In situ* Cu K-edge XANES of CuO-IO catalyst during chronoamperometry from -0.2 V to -1.2 V *vs.* RHE (collected at 30 min at each potential, with comparison to Cu foil standard).

The spectra revealed gradual changes in pre-edge features and white line shifts to lower energy upon potential applications. It indicates that the cupric oxide partially remained in the electrode between -0.2 and -0.4 V and directly reduced to metallic copper as further increasing potentials more negatively.
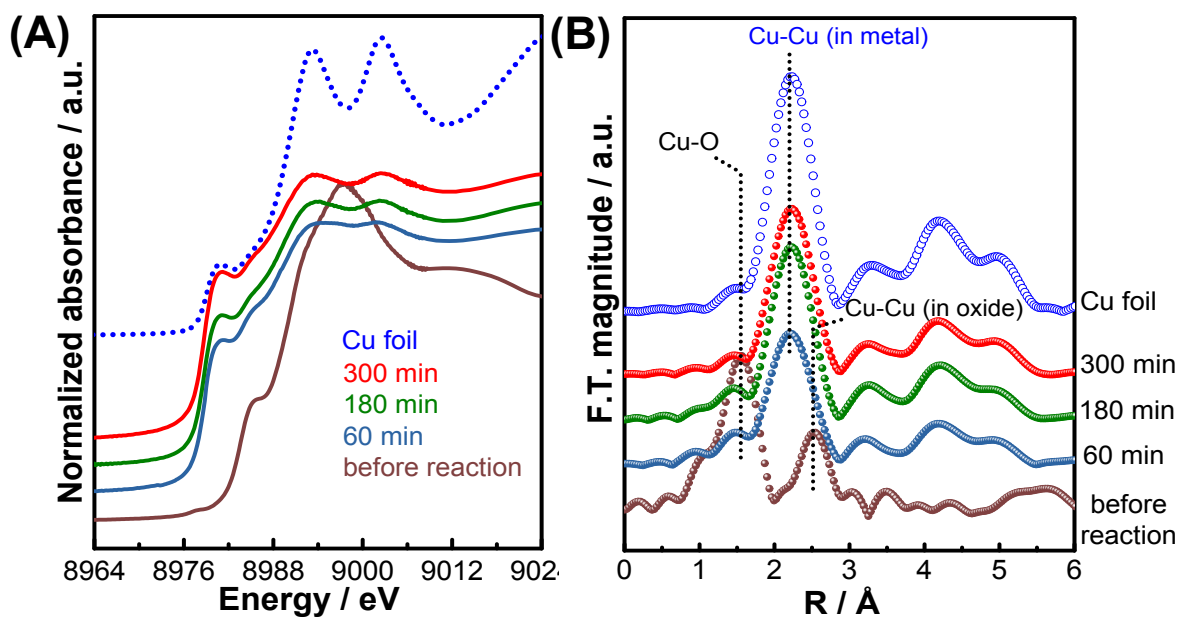
Fig. S24. *In situ* (A) Cu K-edge XANES and (B) EXAFS measurements for real time tracking the oxidation state changes of CuO-IO during EC-CO$_2$RR condition at -0.6 V. The results at steady state are very close to prominent features in Cu foil standard, indicating the reduction of CuO towards metallic copper under working conditions.
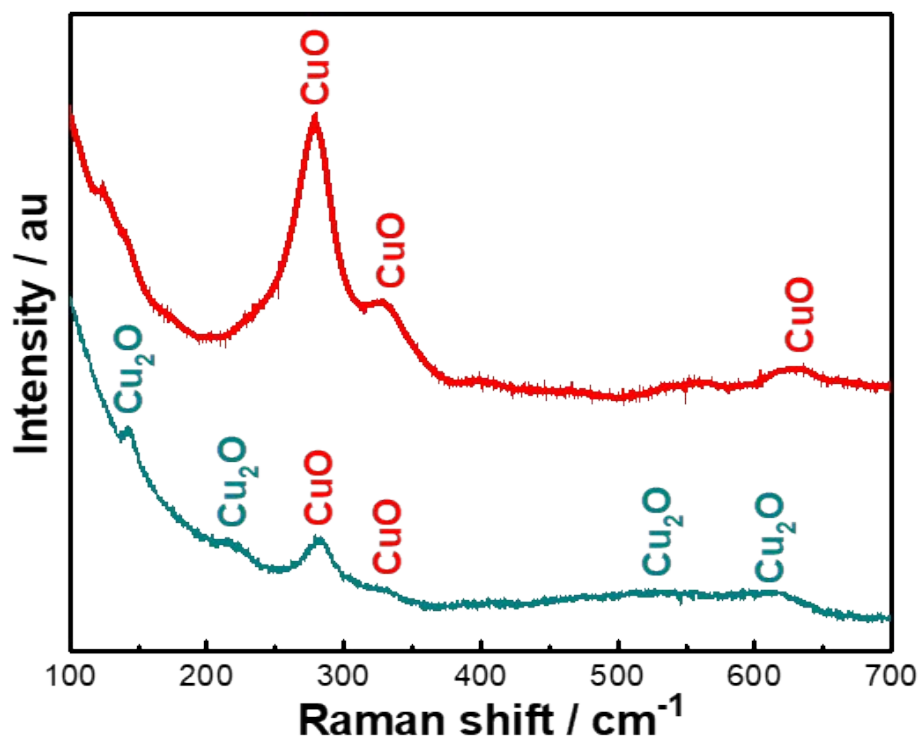
Fig. S25. *Ex situ* Raman spectra of CuO-IO/carbon paper electrodes before (top) and after 24-h durability test at -0.6 V *vs.* RHE (bottom) using 633 nm laser.

Three Raman-active A_g, B_{1g}, and B_{2g} modes were found for fresh CuO-IO electrode (space group C_{2h}^6). After 24-h electrolysis at -0.6 V, apart from small CuO features, two apparent features at lower wavenumbers along with broad peaks in 500-630 cm^{-1} in the post-electrode clearly indicate the presence of additional cubic cuprite Cu_2O (space group O_h^4).
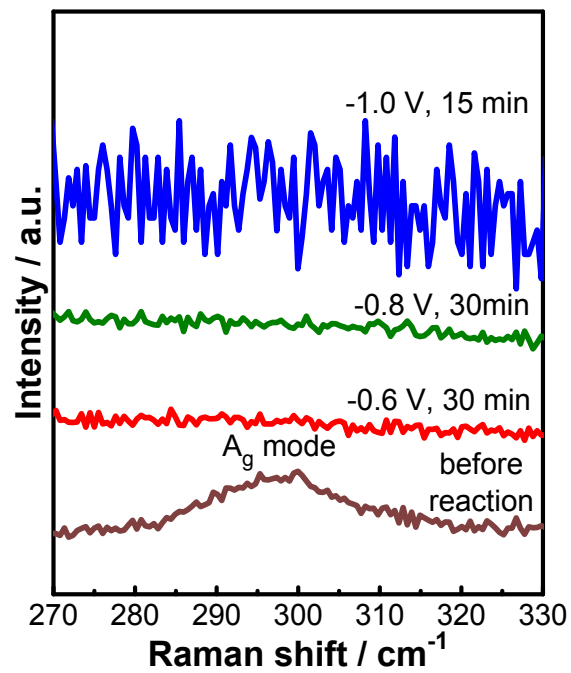
Fig. S26. *In situ* Raman spectra of CuO-IO during EC-CO$_2$RR at various applied potentials (using 785 nm laser source).
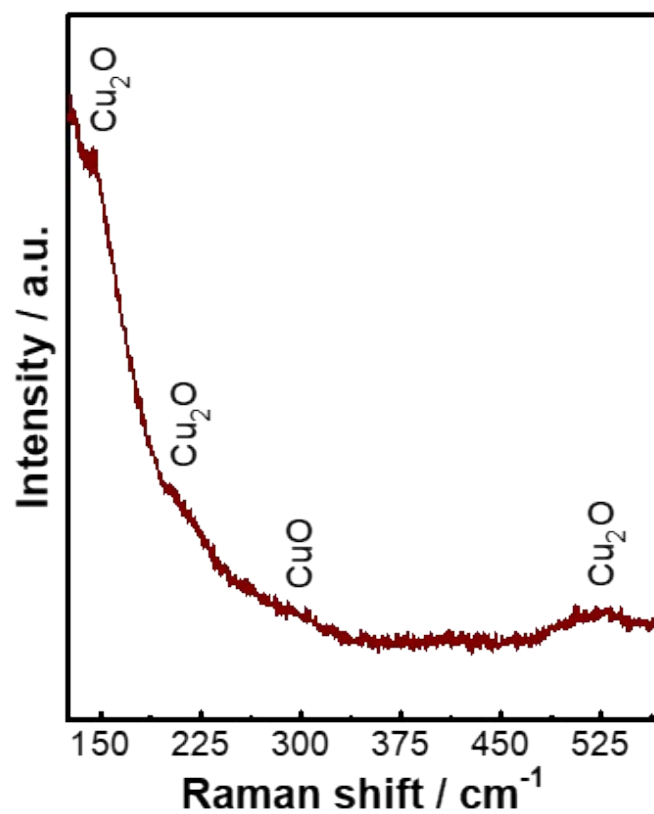
Fig. S27. Raman analysis of CuO-IO collected after CO_2 electrolysis at -0.6 V *vs.* RHE and returned to open circuit (785 nm laser source). This observation is coincident with the *ex situ* measurement in Figure S25.
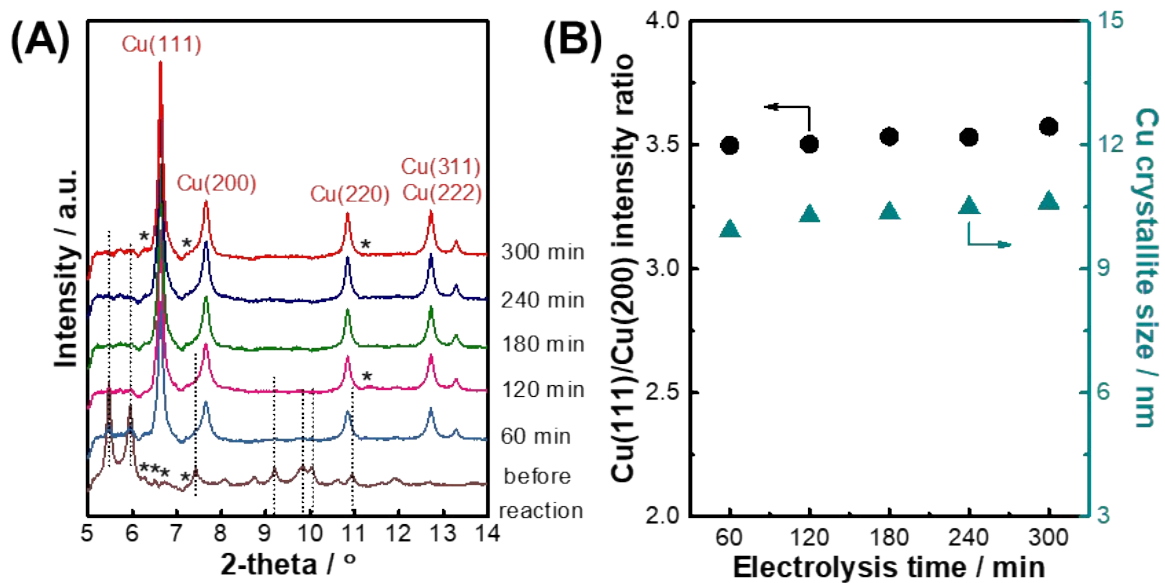
Fig. S28. (A) *In situ* time-resolved SXRD data for tracking the crystallographic changes of CuO-IO from CuO phase under open circuit to metallic Cu during EC-CO$_2$RR at -0.6 V *vs.* RHE (* in (D) indicates residual carbon paper features and Kapton window from background subtraction). (B) Relative peak intensity ratio of Cu (111) and Cu (200) and crystallite size of Cu as a function of electrolysis time showing the consistency over five hours at -0.6 V *vs.* RHE.
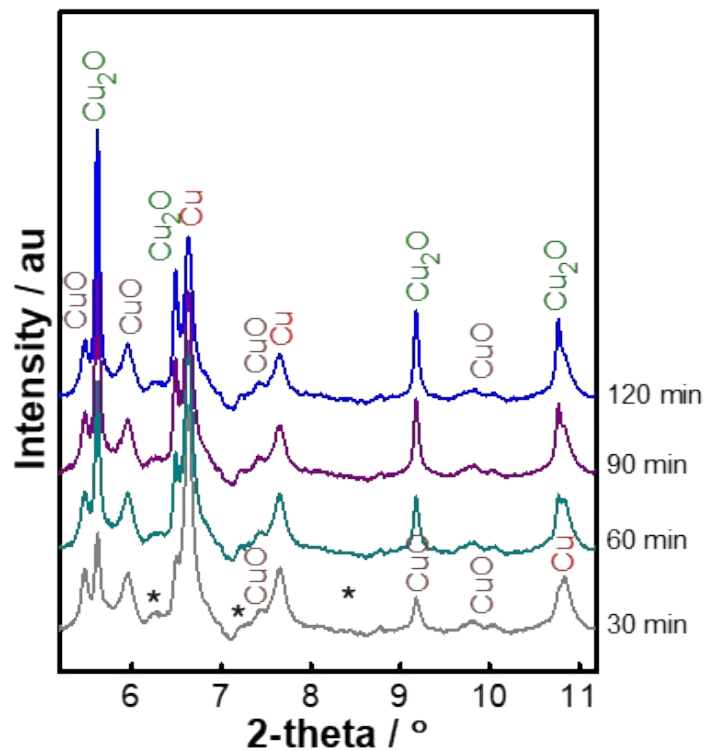
Fig. S29. SXRD patterns of CuO-IO electrode collected after -0.6 V reduction for 5 hours and returned to open circuit for 120 min indicating the gradual re-oxidation of copper to oxide phases over time (* indicates residual carbon paper features from background subtraction).
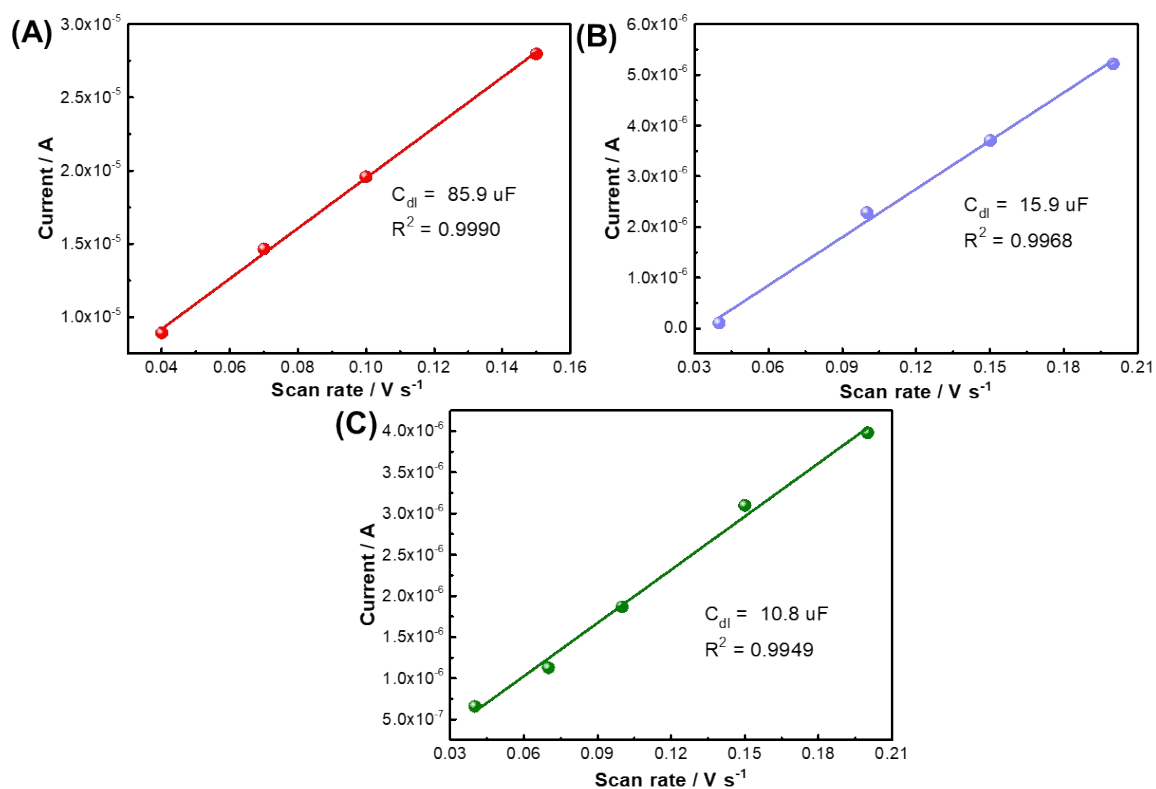
Fig. S30. Non-faradic double layer charging current plotted against scan rate for double layer capacitance estimation for (A) CuO-IO, (B) ~50 nm diameter CuO NPs, and (C) bulk CuO powder electrodes (in CO_2-saturated 0.1 M $KHCO_3$ electrolyte).
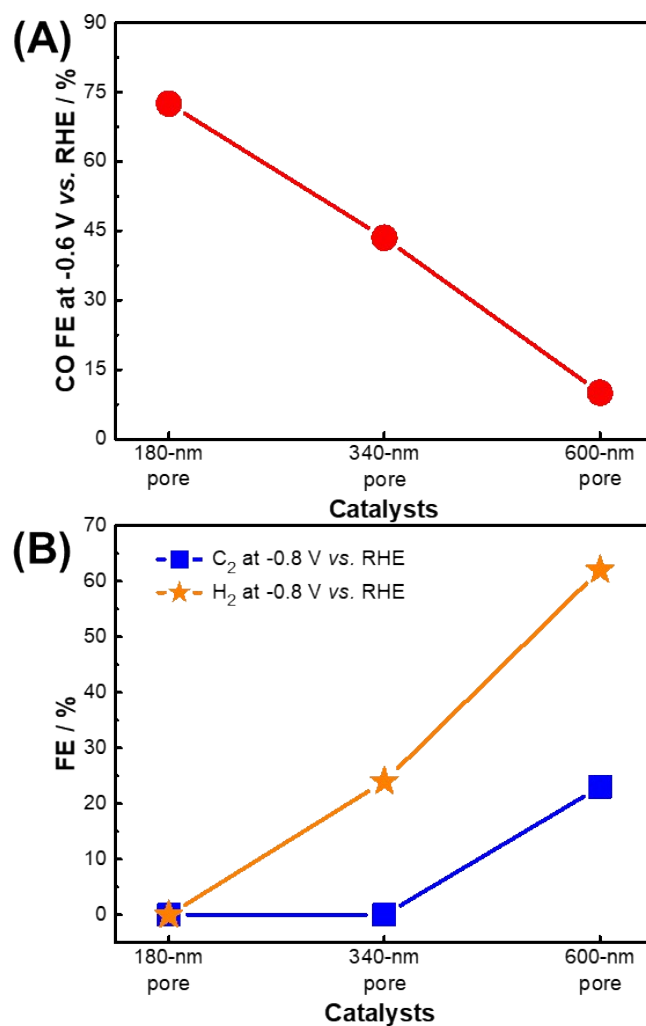
Fig. S31. Comparison of Faradaic efficiency for (A) CO at -0.6 V *vs.* RHE; and (B) average H$_2$ and C$_2$ products at -0.8 V *vs.* RHE between our CuO-IO, Zheng's Cu-IO,[4] and Song's Cu-IO[5] with different macropore sizes.

References

(1).   B. Ravel and M. Newville, *J. Synchrotron Rad.*, 2005, **12**, 537-541.

(2).   C. W. Li and M. W. Kanan, *J. Am. Chem. Soc.*, 2012, **134**, 7231-7234.

(3).   D. Ren, J. Fong and B. S. Yeo, *Nat. Commun.*, 2018, **9**, 925.

(4).   X. Zheng, J. Han, Y. Fu, Y. Deng, Y. Liu, Y. Yang, T. Wang and L. Zhang*, Nano Energy*, 2018, **48**, 93-100.

(5).   H. Song, M. Im, J. T. Song, J.-A. Lim, B.-S. Kim, Y. Kwon, S. Ryu and J. Oh, *Appl. Catal. B*, 2018, **232**, 391-396.